Check for updates

Brittle fragmentation by rapid gas separation in a Hawaiian fountain

Atsuko Namiki [1] ✉, Matthew R. Patrick [2], Michael Manga [3] and Bruce F. Houghton [4]

Brittle fragmentation, generating small pyroclasts from magma, is a key process determining eruptive style. How low-viscosity magma fragments within a rising fountain in a brittle manner, however, is not well understood. Here we describe a fragmentation process in Hawaiian fountains on the basis of observations from the 2018 lower East Rift Zone eruption of Kīlauea Volcano, Hawai'i. The dominant fragmentation mechanism is inertia driven and produces a population of large fluidal pyroclasts. However, when sufficient volcanic gas is released in the fountain, a subpopulation of smaller and more vesicular pyroclasts is generated and entrained into the gas-dominant convective plume. The size distribution of these pyroclasts is similar to that of brittlely fragmented solid materials. The erupted high-vesicularity pyroclasts sometimes preserve a deformed shape. These observations suggest that late-stage rapid expansion lowers the gas temperature adiabatically and cools the outer surface of liquid pyroclasts below the glass transition temperature. The rigid crust fragments as the hot interior attempts to expand due to further volatile diffusion from the melt into bubbles. Adiabatic expansion of volcanic gas occurs in all eruptions. Brittle fragmentation induced by rapid adiabatic cooling may be a widespread process, although of varying importance, in explosive eruptions.

The 2018 lower East Rift Zone eruption of Kīlauea Volcano, Hawai'i, provided a new opportunity to study how low-viscosity magmas can fragment. Voluminous eruption of basaltic magma at fissure 8 (F8) began on 27 May 2018[1,2]. A 30- to 80-m-high fountain fed a 13-km-long lava flow and built an ejecta cone with a radius of approximately 100 m (Extended Data Fig. 1)[1]. Over the lifetime of the fountain, tephra production was highest during the earliest stages and gradually declined through June. Most of the ejecta fell as spatter generated by purely fluid dynamic processes (Methods)[3–6] that produced large droplets and pyroclasts with fluidal shapes (Extended Data Fig. 2). Beyond the cone, there is a more widespread tephra blanket of smaller, more vesicular pyroclasts that we argue are produced by secondary brittle fragmentation.

Brittle fragmentation is a mechanism that effectively generates finer fragments leading to more widespread pyroclast dispersal and thus a more distributed hazard for local communities and infrastructure. Brittle fragmentation can occur if the strain rate is sufficiently large compared with the inverse structural relaxation time of the melt (Methods)[7,8]. The low viscosity of basaltic melt makes it difficult to reach the necessary strain rates, hence basaltic magmas often erupt effusively or in weak explosive eruptions. However, sub-Plinian to powerful Plinian basaltic eruptions can occur[9]. Mechanisms must exist for basaltic magmas to fragment brittlely, despite their low melt viscosity. Phenocrysts and syn-eruptively nucleated microlites can prolong the relaxation time by increasing viscosity[10–12], but the crystallinity of F8 magma is low (Extended Data Fig. 3)[2]. In addition, the eruptive temperature (1,145 °C)[2] is higher than the critical temperature that permits brittle fragmentation by syn-eruptive crystallization (1,100 °C)[12]. External cooling of basaltic magma by atmospheric air or water can generate a rich variety of pyroclast morphologies and internal textures by solidifying the surface, including scoria, golden pumice, reticulite, Pele's hair

and tears, and *Limu O Pele*[13–16]. However, the cause of such efficient cooling in hot basaltic fountains is not obvious.

Here we use the airborne size distributions of erupted pyroclasts and textural observations of tephra to show that a subpopulation of pyroclasts is generated by brittle fragmentation. We then propose that rapid adiabatic gas expansion during the eruption enabled the secondary brittle fragmentation.

Pyroclast size distribution and fountain temperature

Observations of the F8 fountain have been crucial to understanding the process generating pyroclasts (Fig. 1 and Supplementary Video 1). In Fig. 1a, fluidal inertia-driven fragmentation dominates in the core of the fountain, and pyroclasts up to several metres in diameter fall in the vicinity of the fountain to generate the cone and feed a long-lived lava flow. In contrast, Fig. 1b shows an additional cloud of smaller pyroclasts above and beyond the fountain being carried downwind to produce a more dispersed tephra deposit. The size distributions of pyroclasts in Fig. 1a,b differ, suggesting contrasting fragmentation mechanisms (Methods)[17–20].

To reveal the role of magmatic gas in fragmentation, we analysed the relationship between the temperature of the fountain and pyroclast size distribution using infrared images (Methods). We identified the incandescent fountain core (>850 °C; black curve in Fig. 2a,d) and the hot convective gas region surrounding the fountain (>500 °C; white curve in Fig. 2a,d).

When the area of the convective region was large relative to the core, we saw a greater proportion of smaller pyroclasts (Fig. 2c,f,g). In Fig. 2c, the cumulative number of fragments shows a smaller slope for those of radius $L < 0.3$ m, indicating that the radius of efficiently generated pyroclasts was ~0.3 m. This size corresponds to the estimated size of the pyroclasts fragmented fluidally (Methods). In contrast, in Fig. 2f, the size distribution of the smaller pyroclasts with $L < 0.3$ m has a slope $D = 2.1-2.7$, similar to that for brittle

¹Graduate School of Environmental Studies, Nagoya University, Nagoya, Japan. ²US Geological Survey, Hawaiian Volcano Observatory, Hilo, HI, USA. ³Department of Earth and Planetary Science, UC Berkeley, Berkeley, CA, USA. ⁴Department of Earth Sciences, University of Hawaii, Honolulu, HI, USA. ✉e-mail: namiki@eps.nagoya-u.ac.jp

a Coarse pyroclasts   **b** Coarse and fine pyroclasts

Fig. 1 | Time-lapse photographs of F8 fountain. The images were taken within a week of the initiation of sustained fountaining using a visible-light camera with a time interval of 1 s from a site northwest of the vent (yellow and green squares in Extended Data Fig. 1c). **a**, Photographs from 31 May 2018. Erupted magma was disrupted to form coarse pyroclasts that fell in the vicinity of the fountain. **b**, Photographs from 30 May 2018. Smaller pyroclasts were entrained by and transported downwind of the fountain. The wind blew from left to right. The haze in the photographs was produced by volcanic gas. The exact scale in these pictures is ambiguous. The height of the fountain most of the time on 31 May was 50–70 m and occasionally as low as 20 m (L. DeSmither, personal communication).

fragmentation[19,21–26]. We thus conclude that large halos of hot gas were accompanied by the production of smaller pyroclasts.

We also analysed infrared images for 31 May and 4 and 6 June (Extended Data Fig. 4), and found that 8 June (Fig. 2d-f) was the only time that efficiently generated small pyroclasts. Considering this and the observed contrast in behaviour on 30 and 31 May (Fig. 1), special conditions are needed for large numbers of smaller pyroclasts formed by brittle fragmentation.

Pyroclast characteristics and interpretation

Next, we examined the texture of pyroclasts that escaped from the top of the F8 fountain (Fig. 3 and Extended Data Fig. 5). Beneath dense millimetre-thick glassy rinds, the brown interiors had a vesicularity ϕ that exceeded 0.95 (Extended Data Table 1) and a honeycomb structure with a characteristic bubble diameter of ~1 mm,

similar to reticulites[27] (Fig. 3a and Methods). The retraction of disrupted liquid films on the pyroclast surface can thicken the film, becoming the rind.

The texture of the pyroclasts provided an opportunity to understand vesiculation and cooling timescales. The sharp boundary between the porous interior and the denser rind (Fig. 3b,c) suggests that the millimetre-sized bubbles did not originate from secondary vesiculation. Figure 3c shows stretched bubbles that did not have time to relax to a more spherical shape before quenching. Inside pyroclasts, we sometimes found bubbles up to several centimetres in diameter (Extended Data Figs. 5 and 6) that were usually not connected to the pyroclast surface. We thus inferred that the large bubbles resulted from the coalescence of small bubbles. Taken together, these observations implied rapid cooling of the pyroclast surface while the interior cooled slowly enough to provide time for bubbles to coalesce.

Mechanism generating pyroclasts

In the fountain, the characteristic pyroclast size of 0.3 m can be produced by fluidal processes. The smaller and wind-advected pyroclasts are accompanied by a halo of hot gas, raising the possibility of a different fragmentation process. We proposed three mechanisms and properties that together permit brittle fragmentation: (1) gas exsolution and adiabatic cooling, (2) low pyroclast strength and (3) finite elasticity of bubbly magma.

When a highly vesicular magma fragments fluidally, volcanic gas is released from the new surface and rapidly expands (1 in Fig. 4c). Assuming adiabatic expansion, the gas cools the surfaces of the fragmented pyroclasts below the glass transition temperature, enabling the rind to behave in brittle fashion (2 in Fig. 4c and Extended Data Fig. 7a,b). The timescale for thermal diffusion through the 1-mm-thick rind is 1 s (red plus in Fig. 4a and Methods), which is similar to the relaxation timescale of a deformed 1 mm bubble (blue circle in Fig. 4a). The similarity of these timescales is consistent with some deformed bubbles in the rind being quenched in the melt before they relaxed, while other bubbles relaxed to a more spherical shape (Fig. 3b,c).

Cooling a centimetre-sized clast requires a time of $\sim10^2$ s, which permits bubble coalescence in the clast interior (red and yellow circles in Fig. 4a) to form the large bubbles (Extended Data Figs. 5 and 6). Provided the interior of the pyroclasts remains hot, slower diffusion of water from the melt into bubbles continues ($>10^2$ s; green line in Fig. 4a). The maximum amount of dissolved water in the melt depends on the vent pressure, which was 0.1–0.3 wt% at 0.1–1 MPa (Extended Data Fig. 7a,c and Methods).

If the rind has already quenched, the outer shell of pyroclasts cannot expand and volatile diffusion increases pressure (ΔP) inside bubbles (solid curves Fig. 4b). The curves terminate at 1 MPa, because the internal pressure cannot exceed the vent pressure. This pressure produces tensile stresses in the rind. For a clast with radius L and quenched rind thickness δ, the tensile stress on the shell becomes[28] $\Delta P(L-\delta)/(2\delta)$—a thinner shell develops larger stresses. With 0.01 wt% water in the melt fluxed into bubbles, the internal pressure would not exceed the strength of the vesicular magma. However, the stress acting on the thin, solidified rind is one to two orders of magnitude larger and can exceed the low strength of the high-vesicularity magma[29] (dotted and dashed curves in Fig. 4b).

The growth rate of the quenched outer shell depends on the temperature of the gas surrounding the pyroclasts (inset in Fig. 4a). When a pyroclast is surrounded by volcanic gas only slightly colder than the glass transition temperature, the outer shell grows slowly while water diffusion continues because of the high temperature. Thus, the interior of the pyroclast is efficiently pressurized and can rupture the brittle exterior. For colder surrounding gas, the solidified rim grows faster, and the interior of pyroclasts cools more rapidly, with both processes hindering fragmentation.
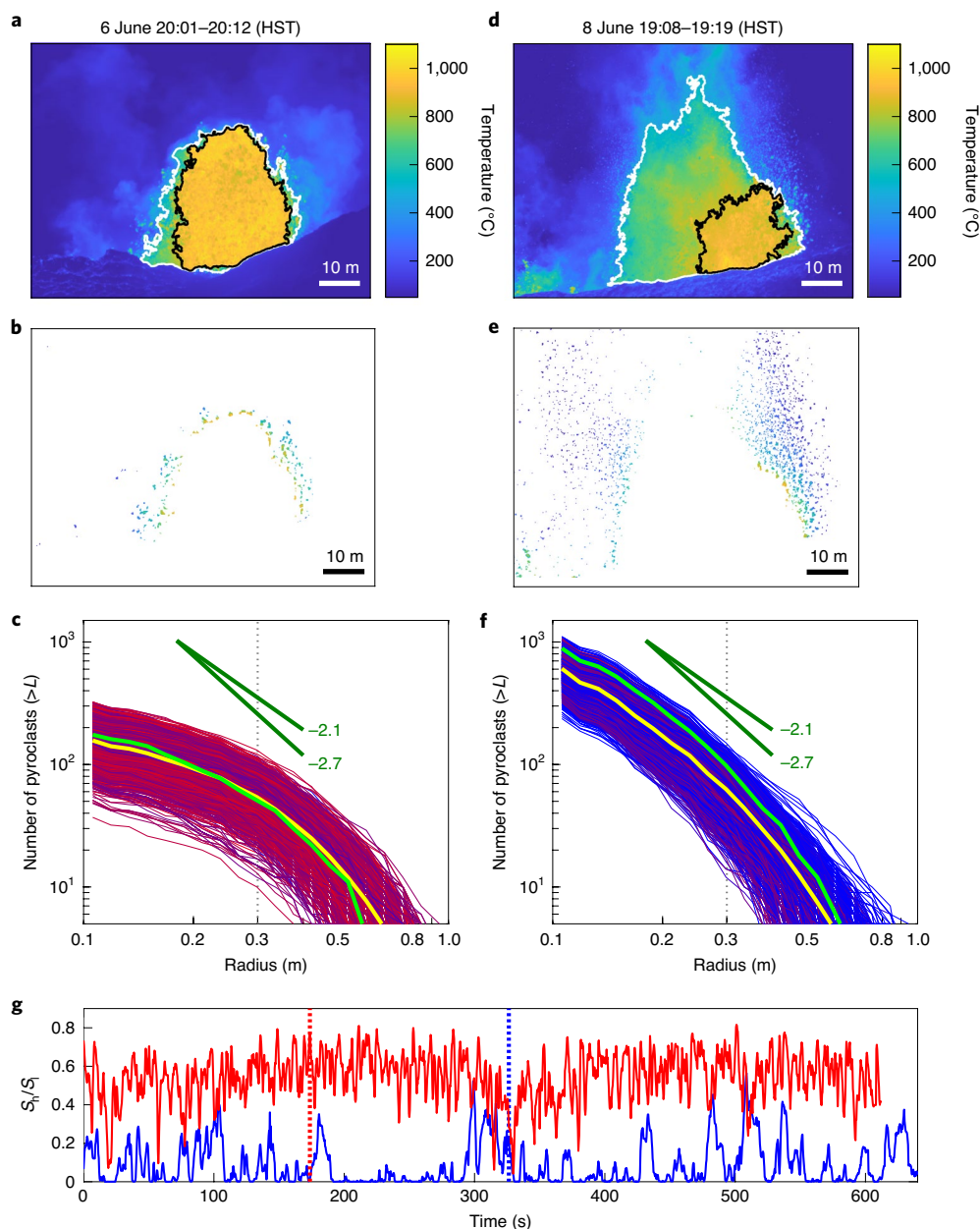
Fig. 2 | Infrared images of the lava fountain and pyroclasts at F8. Images were taken 400 m from the fountain at the yellow square in Extended Data Fig. 1c. **a**, The temperature field observed on 6 June. The black and white contours are isotherms of 850 and 500 °C, respectively. The spatial resolution is 0.08 m per pixel. **b**, The extracted pyroclasts from **a**. The colour scale in **a** also applies to **b**. Pyroclasts located in front of the fountain and inside the hot plume cannot be extracted. **c**, The cumulative number of pyroclasts larger than a certain radius, L, from the 6 June data. Each curve was derived from a single frame across the time span shown in **g**. Reddish and bluish curves indicate the higher and lower ratios of S_h/S_l in **g**. The yellow curve shows the average distribution, and the green curve shows the size distribution for the frame shown in **b**. The dark green lines are references for the slopes. The grey dotted line is a reference for fluidal fragmentation (Methods). **d**–**f**, Same as **a**–**c** but for 8 June. **g**, The areal ratio of the regions at temperatures >850 °C (S_h) and >500 °C (S_l). The vertical dotted lines indicate the times when the photographs in **a** (red) and **d** (blue) were taken. The red and blue curves indicate data for 6 and 8 June, respectively. See Methods for details.

If the vesicularity of the molten interior exceeds the random closed packing of bubbles, which is about 0.64 for uniformly sized spheres and larger for disordered ones, the bubbly magma obtains elasticity by surface tension[30,31]. When the solidified rim fractures, cracks can propagate through the elastic foam to fragment the entire pyroclast (4 in Fig. 4c). In contrast, breadcrust bombs, in which fractures are arrested, generally have vesicularities lower than this threshold[32]. The new molten surfaces quench rapidly, and the process of rupturing can occur again (2–4 in Fig. 4c). If the fragmented

pyroclasts have a rapid relative velocity (>20 m s⁻¹), the collision of fragments causes further brittle fragmentation (Methods). Repeated fragmentation creates smaller fragments through crack propagation, with a size distribution similar to that for brittle fragmentation (Fig. 2f).

We note that this fragmentation mechanism can only occur in a highly vesicular magma. When the vesicularity is low, the bubbly magma behaves as a viscous liquid and will not fracture or generate a cascade of smaller pyroclasts. Field observations indicate that the
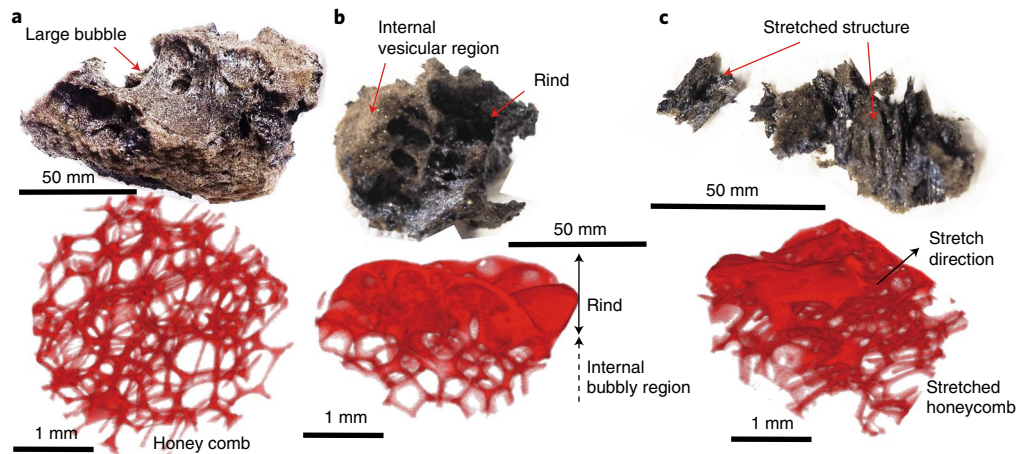
Fig. 3 | Texture analysis of pyroclasts. Top: photographs of entire pyroclasts. A black glassy rind surrounds unbroken portions of the pyroclast. The internal brown region exposed by fracturing shows a structure similar to reticulite or golden pumice. Bottom: corresponding three-dimensional texture projected in two dimensions from X-ray microtomography images of representative subsamples of the pyroclasts. Red shows quenched melt. Thin films surrounding the bubbles were removed to enable the three-dimensional structure to be seen. **a**, High-vesicularity pyroclast with large internal bubbles. The lower image shows the vesicular region with a honeycomb structure with a typical bubble diameter of ~1 mm. **b,c**, Fragments from a single high-vesicularity pyroclast surrounded by a black rind showing undeformed (**b**) and stretched (**c**) bubbles. The maximum thickness of the black rind is 1 mm. The rind is mostly bubble free and only occasionally has small bubbles (<500 μm). See Methods for details.

fountain only occasionally produces small, highly vesicular pyroclasts. Permeable outgassing can reduce the vesicularity locally, and decoupled bubble ascent relative to melt modifies the local and temporal vesicularity. Recycling of outgassed magma within the conduit and rift zone will also lower vesicularity at the vent. The measured vesicularity of the spatter is as low as 0.4 (Extended Data Table 1). In the later phase of the lower East Rift Zone eruption (July 2018), the vesicularity in the lava from F8 fluctuated over time, which may be related to the periodic partial collapses of the Kīlauea summit[33,34]. Thus, it is plausible that the required high vesicularity for promoting brittle fragmentation was only occasionally satisfied at the F8 fountain. Subtle differences in the vesicularity of erupting magma can lead to different fragmentation processes and hence different size distributions.

In the F8 fountain, only a small volume fraction of pyroclasts was produced by brittle fragmentation and dispersed as the widespread fall deposit (Extended Data Fig. 1). However, in other settings, the brittle fragmentation associated with rapid cooling may lead to different eruption dynamics and processes. For example, the eruption of low-viscosity peralkaline rhyolite magma at Aluto caldera in Ethiopia formed pumice cones along with widespread tephra fallout and a column-collapse-fed pyroclastic density current[35]. That is, the fluidally fragmented magma made cones and still generated finer pyroclasts, feeding a hazardous Plinian-type eruption. A cooling experiment with this magma showed that crystallization does not play the main role in triggering fragmentation[36]. Cooling of pyroclasts can arise from contact with a cold atmosphere, but here we argue that cooling can also occur by adiabatic gas release from the erupting bubbly magma. The occurrence of cooling by adiabatic expansion of the gas in rapidly ascending large bubbles has been suggested[37]. Our model suggests that magma cooling by adiabatic expansion occurs on a larger scale and can also cause brittle fragmentation.

Our observations suggest that gas-rich fountains generate a sub-population of smaller and more numerous pyroclasts by secondary fragmentation (Fig. 2). The size distribution of these pyroclasts has a power law in the range of 2.1–2.7, suggesting that they fragmented as a solid. From these observations, we inferred that the surface of large pyroclasts cooled below the glass transition temperature and fractured in a brittle manner. Provided the interior of the pyroclast

is vesicular enough to create elasticity, cracks can propagate through the interior of the pyroclast, creating new, smaller pyroclasts. Our mechanism offers a new explanation for the coexistence of scoria and reticulite in the products of other Hawaiian eruptions[15]. The combination of surface cooling, continued gas exsolution and high vesicularity are necessary conditions for brittle fragmentation of low-viscosity and low-crystallinity melts.

Online content

Any methods, additional references, Nature Research reporting summaries, source data, extended data, supplementary information, acknowledgements, peer review information; details of author contributions and competing interests; and statements of data and code availability are available at https://doi.org/10.1038/s41561-021-00709-0.

References

1. Neal, C. A. et al. The 2018 rift eruption and summit collapse of Kīlauea volcano. *Science* **363**, 367–374 (2019).
2. Gansecki, C. et al. The tangled tale of Kīlauea's 2018 eruption as told by geochemical monitoring. *Science* **366**, eaaz0147 (2019).
3. Eggers, J. & Villermaux, E. Physics of liquid jets. *Rep. Prog. Phys.* **71**, 036601 (2008).
4. Namiki, A. & Manga, M. Transition between fragmentation and permeable outgassing of low viscosity magmas. *J. Volcanol. Geotherm. Res.* **169**, 48–60 (2008).
5. Villermaux, E. The formation of filamentary structures from molten silicates: Pele's hair, angel hair, and blown clinker. *C. R. Mécanique* **340**, 555–564 (2012).
6. Jones, T. J., Reynolds, C. D. & Boothroyd, S. C. Fluid dynamic induced break-up during volcanic eruptions. *Nat. Commun.* **10**, 3828 (2019).
7. Dingwell, D. B. Volcanic dilemma: flow or blow? *Science* **273**, 1054–1055 (1996).
8. Gonnermann, H. M. Magma fragmentation. *Annu. Rev. Earth Planet. Sci.* **43**, 431–458 (2015).
9. Houghton, B. & Gonnermann, H. Basaltic explosive volcanism: constraints from deposits and models. *Geochemistry* **68**, 117–140 (2008).
10. Moitra, P., Gonnermann, H. M., Houghton, B. F. & Tiwary, C. S. Fragmentation and plinian eruption of crystallizing basaltic magma. *Earth Planet. Sci. Lett.* **500**, 97–104 (2018).
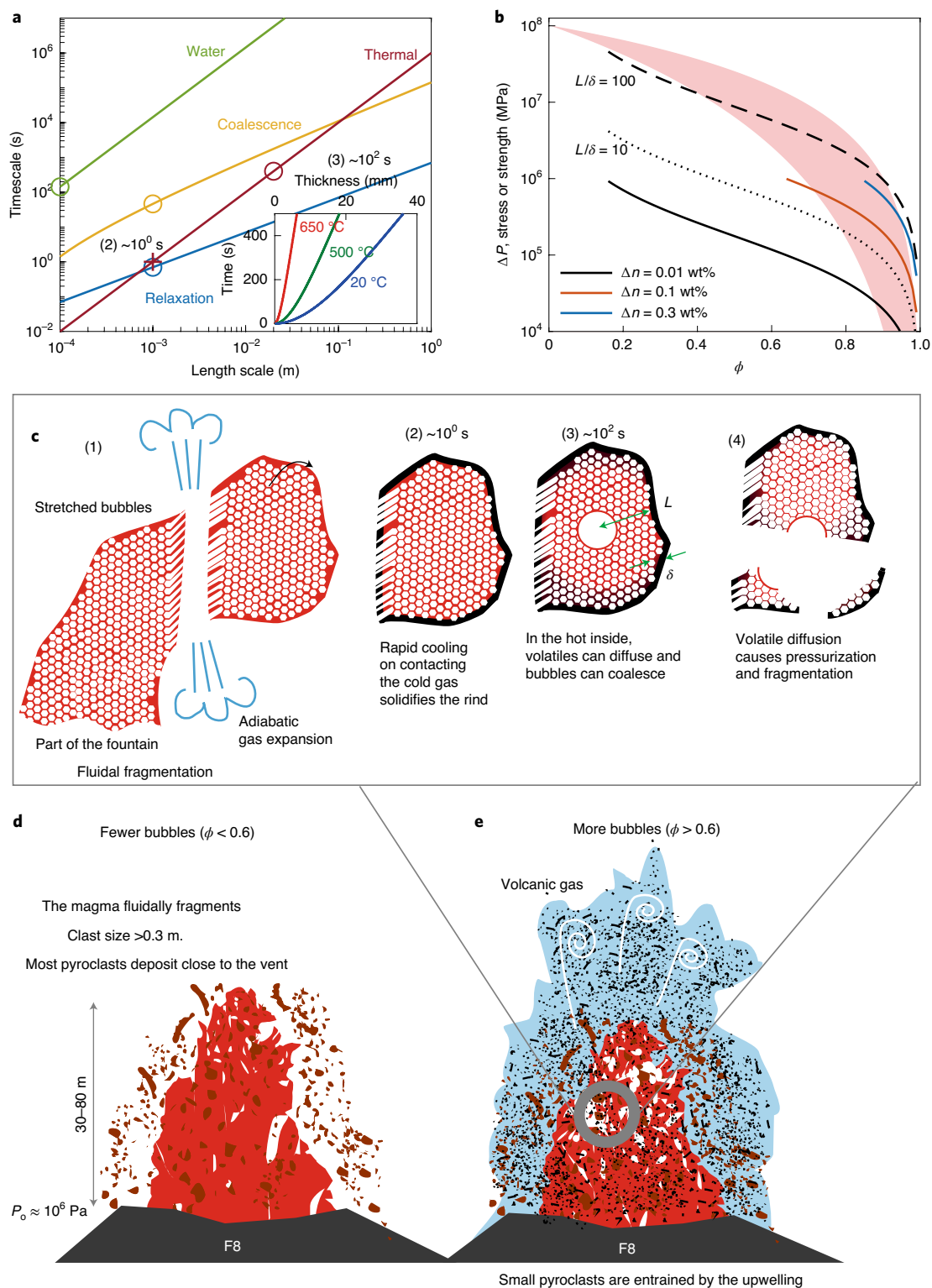
Fig. 4 | Possible mechanisms for generating the smaller pyroclasts. a, Comparison of the various timescales. The curves are the estimated timescales for key processes. The circles and plus sign show representative length and timescales. See text and Methods for details. Labels (2) and (3) correspond to the evolution of pyroclasts shown in **c**. The inset shows the growth in the thickness of the cold rim via cooling below the glass transition temperature through time as a function of the gas–melt interface temperature. **b**, Comparison of strength and the possible stress acting in the rind as a function of vesicularity. Solid curves show the additional pressure ΔP generated by the diffusion of water into bubbles (assuming no gas loss) as a function of the amount of exsolved water, Δn. Dotted and dashed curves show the stresses acting in the quenched rind with a thickness of δ for $\Delta n = 0.01$ wt% produced by water diffusion. The pink region shows the range of strengths of high-vesicularity magmas, which decreases with increasing vesicularity (the required stress for failure)[29]. **c**, Schematic of the evolution of a pyroclast. Labels (1)–(4) show the representative stages and are referred to in the text. **d,e**, Fountains can contain lower-vesicularity (**d**) and higher-vesicularity (**e**) pyroclasts. P_o is a typical pressure at the vent (Extended Data Fig. 7).

11. Spina, L. et al. Gas mobility in rheologically-layered volcanic conduits: the role of decompression rate and crystal content on the ascent dynamics of magmas. *Earth Planet. Sci. Lett.* **524**, 115732 (2019).

12. Arzilli, F. et al. Magma fragmentation in highly explosive basaltic eruptions induced by rapid crystallization. *Nat. Geosci.* **12**, 1023–1028 (2019).

13. Mastin, L. G. Generation of fine hydromagmatic ash by growth and disintegration of glassy rinds. *J. Geophys. Res. Solid Earth* **112**, B02203 (2007).

14. Schipper, C. I., White, J. D. & Houghton, B. F. Syn- and post-fragmentation textures in submarine pyroclasts from Lōʻihi seamount, Hawaiʻi. *J. Volcanol. Geotherm. Res.* **191**, 93–106 (2010).

15. Stovall, W. K., Houghton, B. F., Gonnermann, H., Fagents, S. A. & Swanson, D. A. Eruption dynamics of Hawaiian-style fountains: the case study of episode 1 of the Kīlauea Iki 1959 eruption. *Bull. Volcanol.* **73**, 511–529 (2011).

16. Porritt, L., Russell, J. & Quane, S. Pele's tears and spheres: examples from Kilauea Iki. *Earth Planet. Sci. Lett.* **333-334**, 171–180 (2012).

17. Turcotte, D. L. Fractals and fragmentation. *J. Geophys. Res. Solid Earth* **91**, 1921–1926 (1986).

18. Oddershede, L., Dimon, P. & Bohr, J. Self-organized criticality in fragmenting. *Phys. Rev. Lett.* **71**, 3107–3110 (1993).

19. Domokos, G., Kun, F., Sipos, A. A. & Szabó, T. Universality of fragment shapes. *Sci. Rep.* **5**, 9147 (2015).

20. Fowler, A. C. & Scheu, B. A theoretical explanation of grain size distributions in explosive rock fragmentation. *Proc. R. Soc. A* **472**, 20150843 (2016).

21. Åström, J. A., Ouchterlony, F., Linna, R. P. & Timonen, J. Universal dynamic fragmentation in *D* dimensions. *Phys. Rev. Lett.* **92**, 245506 (2004).

22. Carmona, H. A., Wittel, F. K., Kun, F. & Herrmann, H. J. Fragmentation processes in impact of spheres. *Phys. Rev. E* **77**, 051302 (2008).

23. Kueppers, U., Scheu, B., Spieler, O. & Dingwell, D. B. Fragmentation efficiency of explosive volcanic eruptions: a study of experimentally generated pyroclasts. *J. Volcanol. Geotherm. Res.* **153**, 125–135 (2006).

24. Rust, A. C. & Cashman, K. V. Permeability controls on expansion and size distributions of pyroclasts. *J. Geophys. Res.* **116**, B11202 (2011).

25. Jones, T. J. et al. Primary and secondary fragmentation of crystal-bearing intermediate magma. *J. Volcanol. Geotherm. Res.* **327**, 70–83 (2016).

26. Pioli, L., Bonadonna, C. & Pistolesi, M. Reliability of total grain-size distribution of tephra deposits. *Sci. Rep.* **9**, 10006 (2019).

27. Mangan, M. T. & Cashman, K. V. The structure of basaltic scoria and reticulite and inferences for vesiculation, foam formation, and fragmentation in lava fountains. *J. Volcanol. Geotherm. Res.* **73**, 1–18 (1996).

28. Alidibirov, M. A. A model for viscous magma fragmentation during volcanic blasts. *Bull. Volcanol.* **56**, 459–465 (1994).

29. Namiki, A. et al. Fragility and an extremely low shear modulus of high porosity silicic magma. *J. Volcanol. Geotherm. Res.* **392**, 106760 (2020).

30. Höhler, R. & Cohen-Addad, S. Rheology of liquid foam. *J. Phys. Condens. Matter* **17**, R1041–R1069 (2005).

31. Cohen-Addad, S., Höhler, R. & Pitois, O. Flow in foams and flowing foams. *Annu. Rev. Fluid Mech.* **45**, 241–267 (2013).

32. Wright, H. M. N., Cashman, K. V., Rosi, M. & Cioni, R. Breadcrust bombs as indicators of vulcanian eruption dynamics at Guagua Pichincha volcano, Ecuador. *Bull. Volcanol.* **69**, 281–300 (2007).

33. Anderson, K. R. et al. Magma reservoir failure and the onset of caldera collapse at Kīlauea volcano in 2018. *Science* **366**, eaaz1822 (2019).

34. Patrick, M. R. et al. Cyclic lava effusion during the 2018 eruption of Kīlauea volcano. *Science* **366**, eaay9070 (2019).

35. Clarke, B. et al. Fluidal pyroclasts reveal the intensity of peralkaline rhyolite pumice cone eruptions. *Nat. Commun.* **10**, 2010 (2019).

36. Arzilli, F. et al. Crystallization kinetics of alkali feldspar in peralkaline rhyolitic melts: implications for Pantelleria volcano. *Front. Earth Sci.* **8**, 177 (2020).

37. Oppenheimer, C. et al. Influence of eruptive style on volcanic gas emission chemistry and temperature. *Nat. Geosci.* **11**, 678–681 (2018).

Methods

Fragmentation mechanisms. *Fluidal fragmentation.* In a fountain, ascending magma deforms continuously unless impeded by viscous resistance. If the Reynolds number, a measure of inertia force relative to the viscous resistance, is:

$$\text{Re} = \frac{2L\rho(1-\phi)v}{\eta} > O(1) \qquad (1)$$

the fluid can continue stretching upon eruption and will eventually tear. Here $O(1)$ is a one-order-of-magnitude experimentally determined threshold[4], $\rho \approx 2{,}700\,\text{kg m}^{-3}$ is the melt density, η is viscosity and v is the relative velocity in the fountain, which is several metres per second (Fig. 1).

Although the effective viscosity of bubbly magma depends on bubble fraction and the strain rate, its range is limited[38]. In a fountain deforming at a rapid strain rate, the effective viscosity is similar to that of the melt, $\eta = 250\,\text{Pa s}$ even with high vesicularity $\phi > 0.6$ (Extended Data Fig. 7c,d)[2]. Using representative values $v = 4\,\text{m s}^{-1}$ measured in Fig. 1, $\phi \approx 0.6$ (Extended Data Table 1) and Re = 10 (ref. [4]), we obtain $L \approx 0.3\,\text{m}$. This size is close to the inflection point at 0.3 m in Fig. 2c, where the curve of the size distribution changes.

Surface tension can hinder disruption by preventing stretching but may enable breakup through capillary instabilities. If the ratio of inertial and surface tension stresses, the Weber number[3]

$$\text{We} = \frac{L\rho(1-\phi)v^2}{\Gamma}, \qquad (2)$$

is small enough, surface tension can prevent breakup; here, the surface tension is[39] $\Gamma = 0.36\,\text{N m}^{-1}$. For the pyroclast size observed in the field ($L \approx 10^{-1}\,\text{m}$), a velocity $v > 1\,\text{m s}^{-1}$ and a vesicularity $\phi \approx 0.6$, We $\gg O(10^2)$, indicating that surface tension is not dynamically important.

Criteria for brittle fragmentation. Various criteria for brittle fragmentation have been suggested[8], and they can be understood in a unified way[29] by treating the rheology of bubble- and crystal-free melt as a Maxwell fluid[40]. As discussed in the main text, a sufficiently rapid strain rate $\dot{\epsilon}$ compared with the inverse structural relaxation time of the melt G/η can cause brittle fragmentation, where G is the shear modulus[7,41]. The stress acting on the bubble wall from excess pressure inside bubbles can also cause brittle fragmentation[28,42,43]. Rapid decompression with respect to the relaxation time is another possible process[44].

The maximum stress stored in a deforming Maxwell fluid is $\eta\dot{\epsilon}$. When the viscosity is large, or the strain rate is sufficiently fast, the stress stored in the melt surrounding a bubble can exceed the critical stress for fragmentation $\sigma_\text{c} < \eta\dot{\epsilon}$. A slow decompression yields a slow expansion of bubbly magma, which does not exceed the critical strain rate. Under elastic deformation, stress is a product of shear modulus and strain $G\epsilon$; thus, $\sigma_\text{c} = G\epsilon_\text{c} < \eta\dot{\epsilon}$ is a critical condition, where $\epsilon_\text{c} = 10^{-2} - 10^{-3}$ is the required strain for fragmentation of a silicic magma[29]. A magma deforming at a strain rate $\dot{\epsilon} \gg \sigma_\text{c}/\eta$ behaves like an elastic solid. In a strict sense, when the strain rate is slightly higher than critical for fragmentation $\sigma_\text{c} \approx \eta\dot{\epsilon}$, the melt can experience ductile deformation before fragmentation, which increases the strain before fragmentation. However, the range of strain rates over which both ductile deformation and fragmentation occur is narrow[29].

Thus, the criteria for fragmentation by strain rate, stress and decompression rate lead to the same condition via different expressions. A preferred fragmentation mechanism is chosen by taking account of measurable parameters. We thus used $\eta\dot{\epsilon}$ to show that basaltic melt will not brittlely fragment and used the measured critical stress for the fragmentation of a solidified rind. We assume that is the same order of magnitude as the shear strength measured for 500–950 °C (ref. [29]) because the tensile strength of high-vesicularity magma is not obvious.

Size distribution of fragments. The size distribution of fragments can be diagnostic of the fragmentation mechanism. The cumulative number of fragments N larger than a certain size L often obeys a power law with a slope defined by a fractal dimension D (refs. [17-20]). The mass distribution, frequently used in physics papers, $N(=m) \propto m^{-\tau}$, can be related[17] to the size distribution through $D = 3(\tau - 1)$. Assuming self-similar growth, and the branching and merging of cracks in three dimensions, the theoretical value is $\tau = 5/3$, close to the measured $\tau = 1.7-1.9$ for fragments generated by crack propagation, independent of the material properties and loading conditions[19,21,22]. This range of exponent τ is equivalent to a fractal dimension of $D = 2.1-2.7$; that is, D for brittle fragmentation is in the range of 2.1–2.7.

The value of D for brittle fragmentation does not depend on the impact velocity[45]. In contrast, for fluidal fragmentation, the typical size of the fragments depends on the relative velocity between liquid and gas[46]. When the deformation is plastic, the exponent is[47] $\tau = 1.2$ ($D = 0.6$), smaller than that for brittle fragmentation.

Pyroclasts generated by decompression experiments in a shock tube or by impacts have $D = 2.1-2.6$ (refs. [23,25]), similar to that of the total grain size distribution from explosive eruptions[24,26]. Thus, D may be useful to infer the fragmentation mechanism.

Image analysis. The infrared image in Fig. 2 was obtained by using a FLIR T1030sc camera (1,024 × 768 pixels in the original) with a FOL83mm lens (12°, 0.08 m

per pixel). The frame rate was 30 frames per second, and we analysed every tenth frame (an interval of 1/3 s). In the infrared images, we could identify the regions of the fountain and gas envelope by their shapes, confirmed by observations in visible light (Fig. 1). We tested several threshold temperatures and chose 850 °C and 500 °C as best outlining the fountain and the region of hot gas. The hot gas surrounded the fountain, we thus inferred that the gas was released from magma erupted from the F8 vent.

The pyroclasts in Fig. 2 were extracted from the temperature field by subtracting the average temperature field from the nearest 25 pixels for each pixel. We required the pyroclast to be hotter than the surrounding area, the mean temperature of the pyroclast to be >100 °C to avoid including air temperature fluctuations and larger than 5 pixels in area (the smallest size to avoid artefacts). The timescale for cooling of a pyroclast with a size of 0.1 m is longer than 10^4 s (Fig. 4a), and thus it should remain sufficiently hot to be detected against a cold background. Given that we used hotter anomalies, the detection of pyroclasts located in front of and within the fountain and hot plume was technically challenging. It was difficult to identify the hot and cold anomalies simultaneously. We used the area of the pyroclast to calculate the radius, assuming a circle shape with an equivalent area. The minimum size we could see in Fig. 2b,e was approximately 0.1 m, similar to the largest pyroclasts found in the field outside the spatter cone area. As Fig. 2f shows self-similarity, we assumed that the results obtained in Fig. 2f could be extrapolated to the smaller pyroclasts.

These images were obtained at night. The fountain heights observed by a visible-light camera during the daytime on 6 and 8 June were 30–60 m and 30–70 m, respectively (L. DeSmither, personal communication).

X-ray microtomography. X-ray microtomography was performed on beamline 8.3.2 at the Advanced Light Source, Lawrence Berkeley National Lab. Images were acquired with 25 keV monochromatic X-rays and 200 ms exposure times. A total of 1,313 projections were imaged with a PCO edge camera over a 180° rotation of the sample. Images were 2,560 pixels wide and typically 1,300 pixels tall. Isotropic pixel size was 1.3 μm. Image reconstruction was performed with Xi-cam[48], including centre-of-rotation optimization, along with ring and outlier removal. Segmentation was performed using Fiji with the plug-in Trainable Weka Segmentation; visualization was performed in Fiji after reducing the image resolution by a factor of 10. The pyroclasts imaged were selected to be representative of different pyroclast types and textures.

Timescales and pressurization. The mechanisms leading to fragmentation are controlled by a set of timescales for key processes.

Bubble shape relaxation. The timescale for relaxation of the bubble shape is

$$\tau = \frac{\eta r}{\Gamma}, \qquad (3)$$

where r is bubble radius[6].

Bubble coalescence. The large bubbles observed inside pyroclasts may be generated by the coalescence of smaller bubbles through capillary drainage of the fluid film between bubbles. The timescale for capillary film drainage from an initial thickness of δ_0 to a final thickness of δ_f is

$$\tau_\text{cap} = \xi\log\left(\frac{\delta_0}{\delta_\text{f}}\right)\frac{\eta r}{\Gamma}, \qquad (4)$$

where $\xi = 20$ is an empirical constant and $\delta_\text{f} = 5 \times 10^{-7}\,\text{m}$ (ref. [49]). For the initial film thickness of bubbles, we used an average $\delta_0 = r(\phi^{-1/3} - 1)$ (ref. [50]). For the vesicularity, we used the measured value of $\phi = 0.96$ (Extended Data Table 1). We assumed a constant vesicularity. This assumption was appropriate because the small amount (0.01 wt%) of water diffusion did not notably enhance the originally high vesicularity of pyroclasts, $\phi > 0.6$ (Extended Data Fig. 7d), and the total gas volume in a pyroclast does not change after the solidification of the outer rim.

Thermal and water diffusion. The timescales of diffusion of temperature and water are l^2/diffusivity, where l is the length scale. The thermal diffusivity κ is calculated from the ratio of thermal conductivity over the product of density and heat capacity. The thermal conductivity of the bubbly magma was the volume-weighted average of melt and gas[51], $k_\text{f} = k_\text{m}(1-\phi) + k_\text{a}\phi$, where $k_\text{m} = 1.22\,\text{W m}^{-1}\,\text{K}^{-1}$ was the thermal conductivity of melt[35] and $k_\text{a} = 0.166\,\text{W m}^{-1}\,\text{K}^{-1}$ was the thermal conductivity of steam at 1,200 °C (ref. [52]). For a vesicularity of $\phi = 0.96$, $k_\text{f} = 0.2\,\text{W m}^{-1}\,\text{K}^{-1}$. We here neglected convection and radiation within the individual bubbles because of the small length scale. Heat capacity was calculated by summing the mass fraction gas[35] $C_p = 2{,}300\,\text{J K}^{-1}\,\text{kg}^{-1}$ and melt[53] $C_p = 1{,}500\,\text{J K}^{-1}\,\text{kg}^{-1}$. The thermal diffusivity for $\phi = 0.96$ is $10^{-6}\,\text{m}^2\,\text{s}^{-1}$.

For the diffusivity of water we use $7 \times 10^{-11}\,\text{m}^2\,\text{s}^{-1}$, a value for a melt with 0.2 wt% water at 1,145 °C (refs. [54,55]).

Growth of solidified crust. In the inset of Fig. 4a, we solved the diffusion equation for a spherical geometry to obtain the thickness at the solidified surface of the pyroclasts. We assumed a pyroclast with a radius of 0.1 m, thermal diffusivity of $10^{-6}\,\text{m}^2\,\text{s}^{-1}$, initial

temperature of 1,145 °C and contact with the atmosphere or gas at temperatures of 20 °C, 500 °C and 650 °C. We here assumed that the surface temperature of the pyroclast was the same as the surrounding gas because the time until the surface temperature of the pyroclasts became equal to the surrounding gas was relatively short[56]. This assumption maximized cooling at the surface. For a glass transition temperature of basaltic magma, we assume 700 °C (refs. [53,57]).

Pressurization in pyroclasts. From the equation of state of an ideal gas, when an amount of steam ΔN (in mol) is added into a bubble with constant volume V_g and temperature T, the pressure increase is $\Delta P V_g = \Delta N R_g T$, where $R_g = 8.3\,\mathrm{J\,mol^{-1}K^{-1}}$ is the universal gas constant. Using the melt volume of V_m, the newly added steam is written as $\Delta N = (\Delta n/100)\rho V_m/M$, where Δn wt% is exsolved water from the melt and M is the molar weight of water. The volume ratio of melt and gas is written as $V_m/V_g = (1/\phi - 1)$, thus $\Delta P = (\Delta n/100)\rho(1/\phi - 1)(R_g/M)T$, where $R_g/M = 461\,\mathrm{J\,kg^{-1}K^{-1}}$ is the gas constant for steam (Fig. 4b).

Conditions in the fountain. *Pressure range at the vent.* Large pyroclasts will be approximately ballistic and their velocity near the vent can be estimated from the fountain height h as $v \approx \sqrt{2gh}$, where $g = 9.8\,\mathrm{m\,s^{-2}}$ is the gravitational acceleration[58]. From Bernoulli's equation, the source pressure is $P_o \approx \rho(1-\phi)v^2/2 \approx \rho(1-\phi)gh$.

Gas cooling by expansion. The temperature drop by adiabatic expansion of the volcanic gas from P_o to the atmospheric pressure $P_g \approx 10^5\,\mathrm{Pa}$ is estimated from

$$T_g = T_o \left(\frac{P_g}{P_o}\right)^{(\gamma-1)/\gamma}, \qquad (5)$$

where $\gamma \approx 1.34$ is the specific heat ratio for steam[59]. In Extended Data Fig. 7b, we use the pressure in Extended Data Fig. 7a as P_o. The initial gas temperature should equal that of the magma $T_o = 1,145\,°C$ (ref. [2]). The expansion of inviscid gas should be fast compared with the other timescales estimated in Fig. 4a (refs. [28,60]).

Several mechanisms exist for separating volcanic gas in bubbles from the surrounding melt to cause adiabatic cooling. The fluidal fragmentation of magma releases the gas in the bubbles contacting the fragmented surface (Fig. 4c). In a high-vesicularity and low-viscosity magma, once bubble coalescence occurs by film rupture, the rupture can cascade to the surrounding bubbles, which creates large void spaces rapidly and releases volcanic gas efficiently[61]. The differential velocity of bubbles in ascending magma promotes coalescence, which also causes rapid gas separation[37].

The possibility of fragmentation by collisions of particles. If kinetic energy of the pyroclast is converted into elastic energy during collisions, the stress of σ is estimated by $\rho(1-\phi)v^2/2 = \sigma^2/(2E)$. The Young's modulus for highly vesicular magma is uncertain but should be the same order of magnitude as the shear modulus of $10^7\,\mathrm{Pa}$ (ref. [29]). Assuming $\phi > 0.9$, the stress required for fragmentation $\sigma > 10^6\,\mathrm{Pa}$ (Fig. 4). Relative velocities of $>20\,\mathrm{m\,s^{-1}}$, are sufficient to fragment colliding pyroclasts.

Data availability
The movie used for Fig. 1 is Supplementary Video 1; movies used for Fig. 2, CT data and pictures of reticulites are available at https://doi.org/10.17605/OSF.IO/4UVYQ.

Code availability
To create Figs. 2 and 4 and Extended Data Fig. 7, we used MATLAB 9.5. The MATLAB scripts used for the calculations are available from the corresponding author upon request. The CT data in Fig. 3 was analysed using Fiji Is Just ImageJ (https://imagej.net/Fiji) with the Trainable Weka Segmentation plug-in (https://imagej.net/Trainable_Weka_Segmentation).

References
38. Rust, A. C. & Manga, M. Effects of bubble deformation on the viscosity of dilute suspensions. *J. Non-Newton. Fluid* **104**, 53–63 (2002).
39. Walker, D. & Mullins, O. Surface tension of natural silicate melts from 1,200°-1,500 °C and implications for melt structure. *Contrib. Mineral. Petrol.* **76**, 455–462 (1981).
40. Dingwell, D. B. & Webb, S. L. Structural relaxation in silicate melts and non-Newtonian melt rheology in geologic processes. *Phys. Chem. Minerals* **16**, 508–516 (1989).
41. Papale, P. Strain-induced magma fragmentation in explosive eruptions. *Nature* **397**, 425–428 (1999).
42. McBirney, A. R. & Murase, T. Factors governing the formation of pyroclastic rocks. *Bull. Volcanol.* **34**, 372–384 (1970).
43. Zhang, Y. A criterion for the fragmentation of bubbly magma based on brittle failure theory. *Nature* **402**, 648–650 (1999).
44. Kameda, M. et al. Advancement of magma fragmentation by inhomogeneous bubble distribution. *Sci. Rep.* **7**, 16755 (2017).
45. Timár, G., Kun, F., Carmona, H. A. & Herrmann, H. J. Scaling laws for impact fragmentation of spherical solids. *Phys. Rev. E* **86**, 016113 (2012).
46. Villermaux, E. & Bossa, B. Single-drop fragmentation determines size distribution of raindrops. *Nat. Phys.* **5**, 697–702 (2009).
47. Timár, G., Blömer, J., Kun, F. & Herrmann, H. J. New universality class for the fragmentation of plastic materials. *Phys. Rev. Lett.* **104**, 095502 (2010).
48. Pandolfi, R. J. et al. Xi-cam: a versatile interface for data visualization and analysis. *J. Synchrotron Radiat.* **25**, 1261–1270 (2018).
49. Nguyen, C. T. et al. Film drainage and the lifetime of bubbles. *Geochem. Geophys. Geosyst.* **14**, 3616–3631 (2013).
50. Princen, H. M., Aronson, M. P. & Moser, J. C. Highly concentrated emulsions. II. Real systems. The effect of film thickness and contact angle on the volume fraction in creamed emulsions. *J. Colloid Interface Sci.* **75**, 246–270 (1980).
51. Gibson, L. J & Ashby, M. F. *Cellular Solids: Structure and Properties* 2nd edn (Cambridge Univ. Press, 1997).
52. *Thermophysical Properties Database System* (AIST, 2020); https://tpds.db.aist.go.jp/tpds-web/index.aspx?MaterialID=6515
53. Di Genova, D., Romano, C., Giordano, D. & Alletti, M. Heat capacity, configurational heat capacity and fragility of hydrous magmas. *Geochim. Cosmochim. Acta* **142**, 314–333 (2014).
54. Zhang, Y. & Stolper, E. M. Water diffusion in a basaltic melt. *Nature* **351**, 306–309 (1991).
55. Okumura, S. & Nakashima, S. Water diffusion in basaltic to dacitic glasses. *Chem. Geol.* **227**, 70–82 (2006).
56. Benage, M. C. et al. Tying textures of breadcrust bombs to their transport regime and cooling history. *J. Volcanol. Geotherm. Res.* **274**, 92–107 (2014).
57. Ryan, M. P. & Sammis, C. G. The glass transition in basalt. *J. Geophys. Res. Solid Earth* **86**, 9519–9535 (1981).
58. Wilson, L. & Head, J. W. III. Ascent and eruption of basaltic magma on the earth and moon. *J. Geophys. Res. Solid Earth* **86**, 2971–3001 (1981).
59. Harashima, A. *Thermodynamics, Statistical Mechanics* (in Japanese) (Baifukan, 1978).
60. Wilson, L., Sparks, R. S. J. & Walker, G. P. L. Explosive volcanic eruptions — IV. The control of magma properties and conduit geometry on eruption column behaviour. *Geophys. J. R. Astron. Soc.* **63**, 117–148 (1980).
61. Namiki, A. & Kagoshima, T. Intermittent and efficient outgassing by the upward propagation of film ruptures in a bubbly magma. *J. Geophys. Res. Solid Earth* **119**, 919–935 (2014).
62. Newman, S. & Lowenstern, J. B. VolatileCalc: a silicate melt-H_2O-CO_2 solution model written in Visual Basic for excel. *Comput. Geosci.* **28**, 597–604 (2002).
63. Ferguson, D. J. et al. Magma decompression rates during explosive eruptions of Kīlauea volcano, Hawai'i, recorded by melt embayments. *Bull. Volcanol.* **78**, 71 (2016).
64. Shea, T. et al. Textural studies of vesicles in volcanic rocks: an integrated methodology. *J. Volcanol. Geotherm. Res.* **190**, 271–289 (2010).

Author contributions
M.R.P. recorded the visible and infrared movies, M.M. obtained the CT data and A.N. analysed both datasets. B.F.H. interpreted them in the context of the eruption dynamics. A.N. and M.M. wrote the manuscript. All authors discussed the results and contributed to preparing the manuscript.

Competing interests
The authors declare no competing interests.

Additional information
Extended data is available for this paper at https://doi.org/10.1038/s41561-021-00709-0.

Supplementary information The online version contains supplementary material available at https://doi.org/10.1038/s41561-021-00709-0.

Correspondence and requests for materials should be addressed to A.N.

Peer review information *Nature Geoscience* thanks Laura Spina and the other, anonymous, reviewer(s) for their contribution to the peer review of this work. Primary Handling Editor: Rebecca Neely.

**Reprints and permissions information** is available at www.nature.com/reprints.
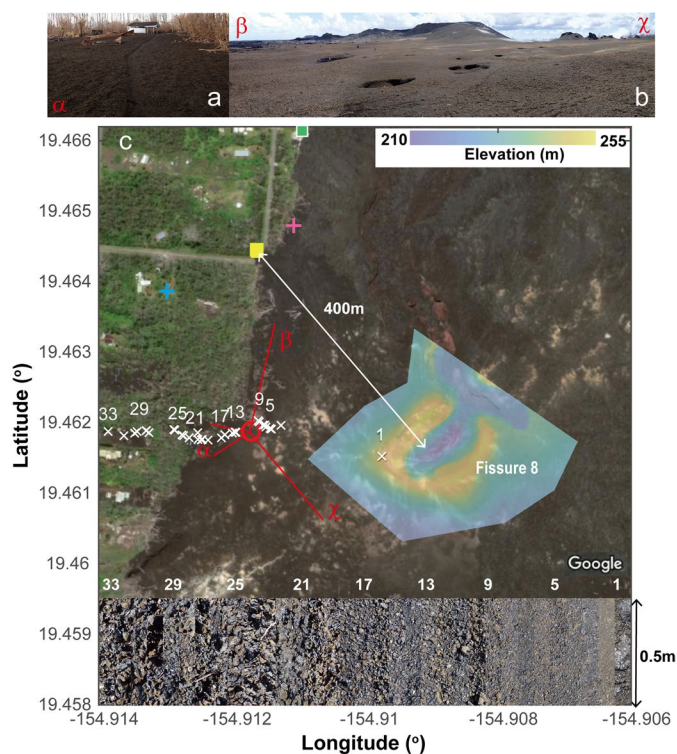
Extended Data Fig. 1 | Map around the F8 cone. a,b, Panoramic view from the location marked by the red circle in (**c**) taken on September 16th, 2018. The view angle is denoted by characters $\alpha - \chi$ in (**c**). **c**, Photo around the F8 cone downloaded from Google Earth in June 2020. The bluish region is the overlay of the digital elevation map around the F8 cone created from thermal images acquired during a helicopter overflight on August 15th, 2018. The yellow square and green square with white rim are the location where the photos in Figs. 1a, 2, and 1b were taken, respectively. The red circle and blue plus indicate the sites where samples in Fig. 3a,b-c are collected, respectively. **d**, Pictures of the ground surface in a region 0.5 m × 75 mm taken in August 2018. The numbers correspond to the locations denoted by × in (**c**). The location close to the vent (×1 in c) is covered by silvery spatter. Sites close to the cone (×2-16) were initially covered by lava flows, then covered by broken reticulite, Pele's hairs, and tears. The typical size of the pyroclasts is smaller than 50 mm. The locations west of number 17 are covered by large (>50 mm) reticulite with a black rind that erupted during the fountaining. The volume ratio of the widespread tephra/cone for F8 has not yet been reported but based on the 1959 Kīlauea Iki cone with similar dimensions to the F8 cone, the volume fraction of F8 widespread tephra is as low as 2%.
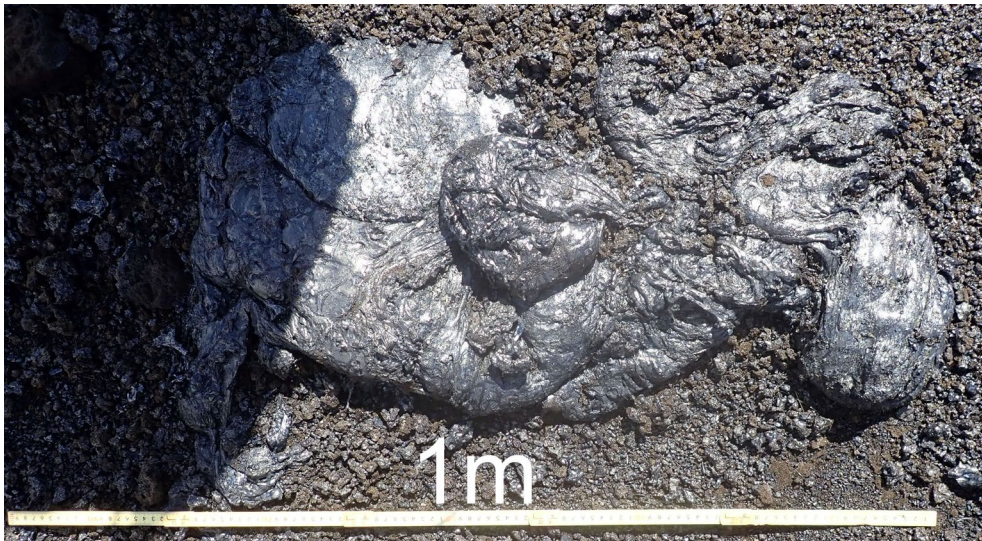
Extended Data Fig. 2 | A large spatter clast. A large spatter clast close to the vent (×1 in Extended Data Fig. 1c).
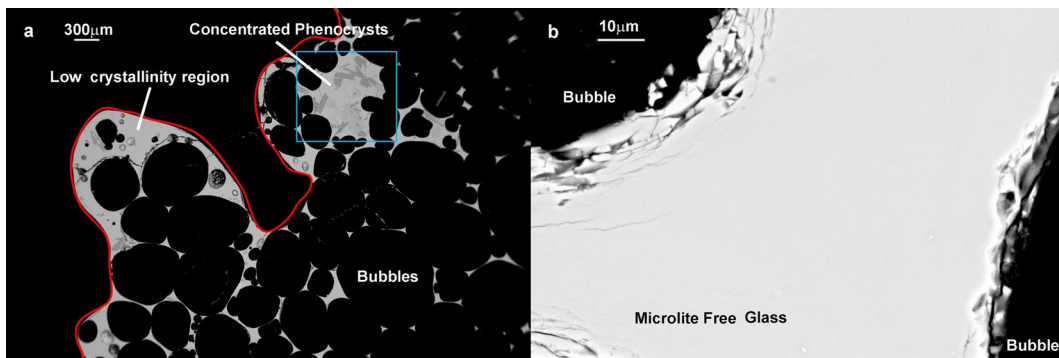
Extended Data Fig. 3 | SEM images of pyroclasts. Back-Scatter Electron (BSE) Scanning Electron Microscope (SEM) images of pyroclasts from F8 shown in Fig. 3b. Images were collected at 20kV on a Zeiss EVO-10 Variable Vacuum SEM at the University of California, Berkeley. **a**, A wide field of view shows that crystallinity is low except for the region with clusters of phenocrysts (for example, blue rectangle). The area fraction of crystals in the blue rectangle is 25 %. The outer rim of the sample outlined by the red curve, which experienced fragmentation, contains few crystals. **b**, Magnified image shows the microlite free glass between bubbles.
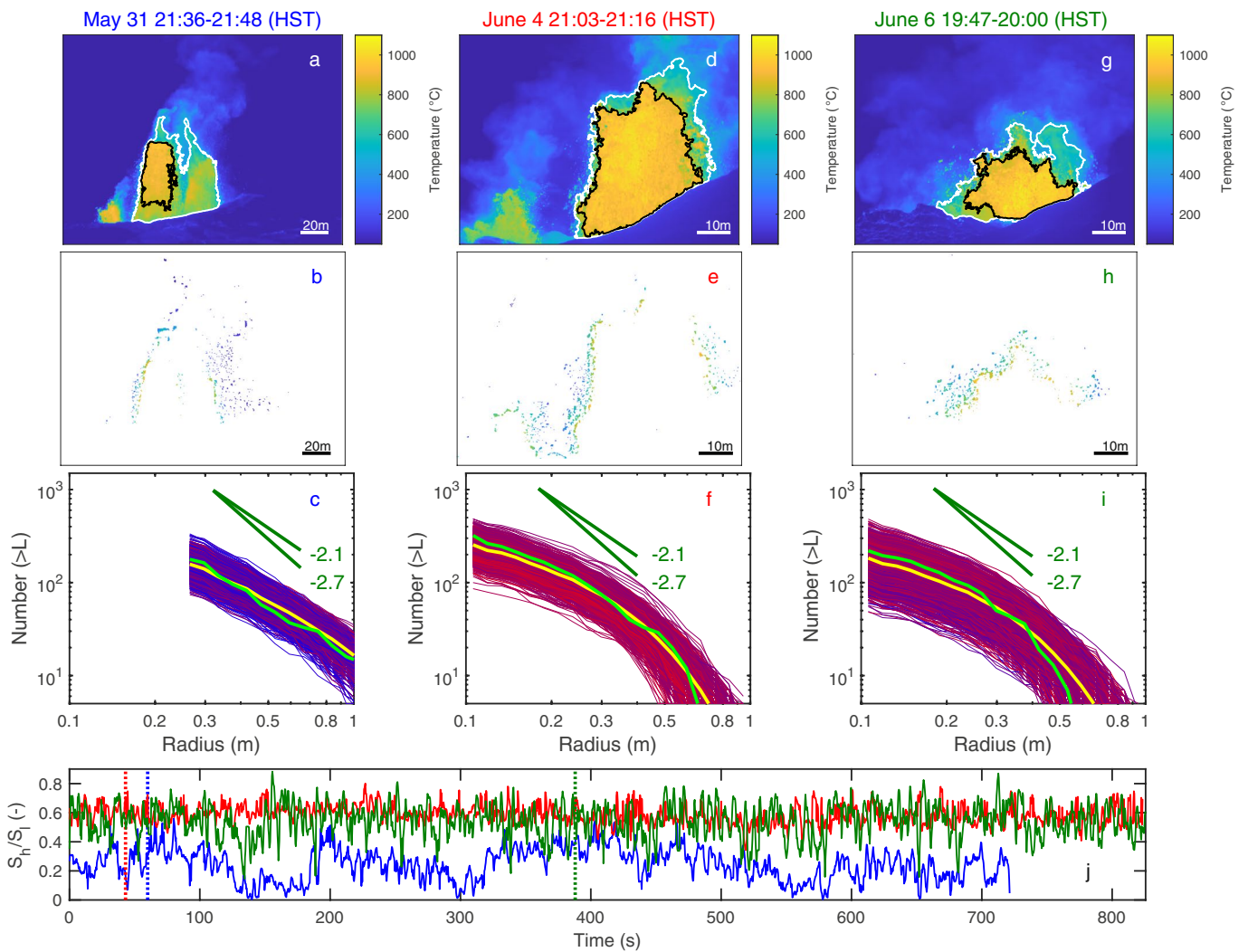
Extended Data Fig. 4 | Infrared data for other time spans. Same as Fig. 2, but for other time spans. On 4 and 6 June (19:47-20:00), the fountain shows similar trends observed in Fig. 2a-c, 6 June (20:01-20:12). On 31 May, (a-c and blue curve in j), we used another lens (FOL36mm lens, 28°), and the spatial resolution is 0.19 m/pixel. Thus it is difficult to compare with other data directly. However, the areal ratio S_h/S_l is lower than on 4 and 6 June, but higher than 8 June.
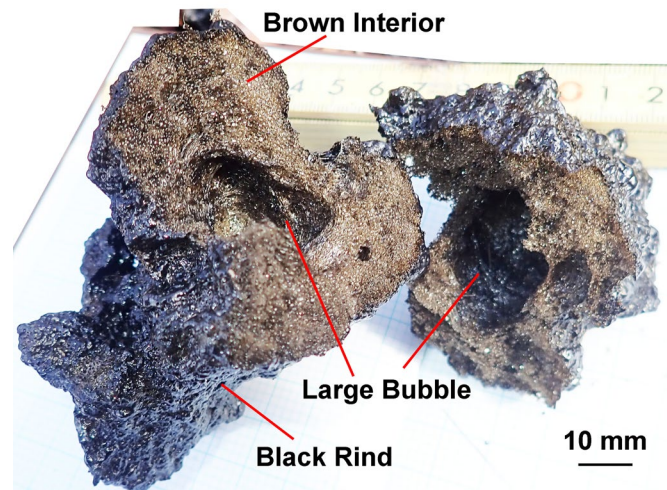
Extended Data Fig. 5 | Example of one pyroclast from the tephra deposit. The right and left parts were initially connected. To show the interior, we broke a pyroclast entirely coated by a black glassy rind. The internal brown region is made of small bubbles. A large bubble exists in the middle of the pyroclast. This photograph is taken on August 9th at the location denoted by blue plus in Extended Data Fig. 1.
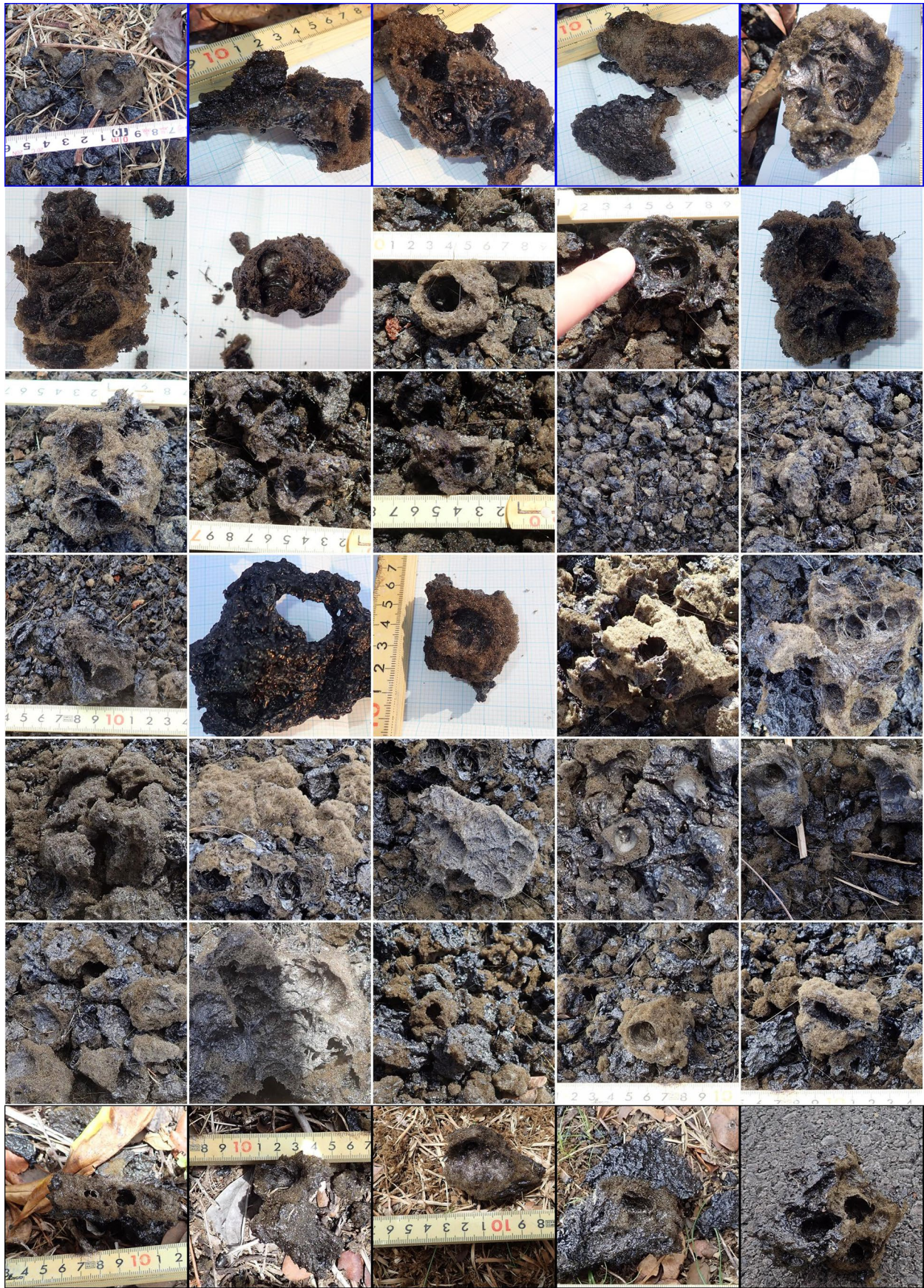
Extended Data Fig. 6 | See next page for caption.

Extended Data Fig. 6 | A collection of photographs of the high vesicularity pyroclasts. A collection of photographs of the high vesicularity pyroclasts including large bubbles (∼ 20-30 mm). The size of each picture is approximately 0.1×0.1 m^2. The edge color of each panel indicates the image locations of samples; blue and whites correspond to blue + and around the white × in Extended Data Fig. 1, and black indicates 1.6 km west-southwest from the F8 vent. The photographs are taken from July - September 2018.
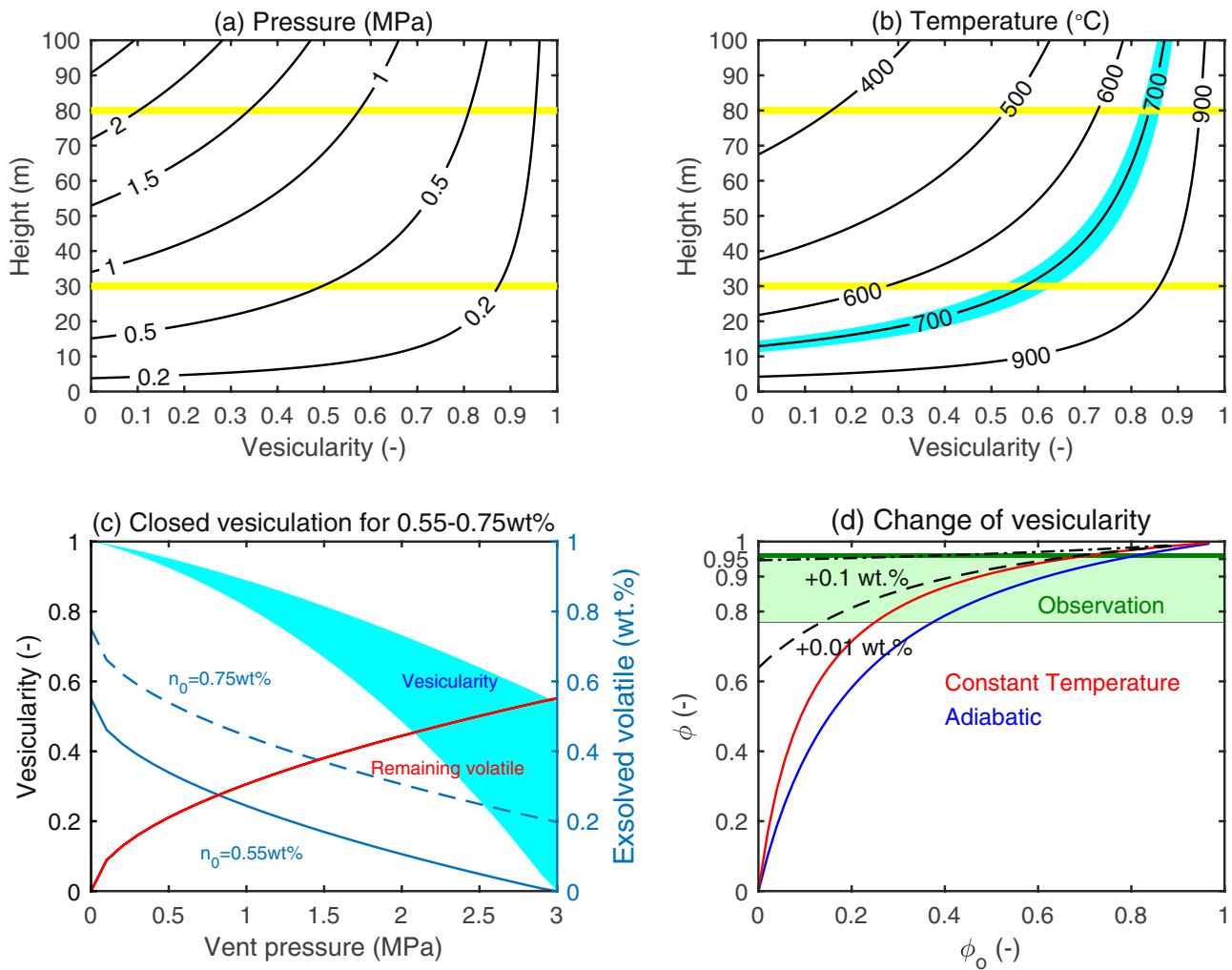
Extended Data Fig. 7 | Estimated conditions around the vent. a, The vent pressure estimated from fountain height and magma vesicularity. Yellow lines identify the observed range of fountain heights, 30-80 m. **b**, The estimated gas temperature following adiabatic expansion by the pressure reduction from (a). The blue region indicates the glass transition temperature of 680-730 °C[53,57]. **c**, Estimated vesicularity range from the solubility of water in a basaltic magma[62]. The initial volatile fraction of the LERZ magma is not yet known, but that for other similar fountains is estimated to be 0.55-0.75 wt.%[63], which we used. The blue curves and region show exsolved volatile fraction and vesicularity at the vent, respectively. The red curve shows the remaining volatiles in the melt. We here do not consider CO_2, because the estimated CO_2 fraction of 170-400 ppm[63] is sufficiently smaller than water, and CO_2 bubbles exsolved deeper may behave differently from steam bubbles. **d**, Vesicularity of pyroclasts. The blue and red curves show the vesicularity change from ϕ_o to ϕ by adiabatic and constant temperature decompression, respectively, from 10^6 Pa to 10^5 Pa. We here use 10^6 Pa as a typical estimate based on (a). The black dashed and dot-dashed curves show the porosity increases by the additional exsolution of 0.01 wt.% and 0.1 wt.% water, respectively. The green shaded region indicates the measured porosity of fall deposited pyroclasts. Estimated vesicularities in (**c,d**) and pressure in (**a**) suggest that the magma in the fountain can have a porosity > 0.6, if the separation of gas and melt was not efficient. See Methods for details.

Sampling site	Inside	Whole
Blue +	0.95	0.94
Pink +		0.76
White ×5	0.96	0.93
White ×5	0.96	0.95
White ×1		0.41
White × 1		0.42

Extended Data Table 1 | Measured vesicularities depending on the location of the pyroclasts. The sampling sites indicate the markers denoted in Extended Data Fig. 1. To obtain the vesicularity, we measured the mass and volume of pyroclasts. To measure the volume, we coated the pyroclasts with a paraffin film and immersed within water. The volume of the solid part is calculated by the mass of the pyroclasts and the density of the solid part, which was obtained by weighing and measuring the volume of the powdered pyroclasts using a pycnometer[64].